Research Article | Vol. 14, No. 9 / 1 Sep 2023 / Biomedical Optics Express 4660
Biomedical Optics EXPRESS

Humanoid-shaped WaveFlex biosensor for the detection of food contamination

RAGINI SINGH,[1] WEN ZHANG,[2] XUECHENG LIU,[2] BINGYUAN ZHANG,[2,3] AND SANTOSH KUMAR[2,*]

[1]College of Agronomy, Liaocheng University, Liaocheng 252059, China
[2]Shandong Key Laboratory of Optical Communication Science and Technology, School of Physics Science and Information Technology, Liaocheng University, Liaocheng 252059, China
[3]zhangbingyuan@lcu.edu.cn
[*]santosh@lcu.edu.cn

Abstract: High-toxicity secondary metabolites called aflatoxin are naturally produced by the fungus *Aspergillus*. In a warm, humid climate, *Aspergillus* growth can be considerably accelerated. The most dangerous chemical among all aflatoxins is aflatoxin B1 (AFB1), which has the potential to cause cancer and several other health risks. As a result, food forensicists now urgently need a method that is more precise, quick, and practical for aflatoxin testing. The current study focuses on the development of a highly sensitive, specific, label-free, and rapid detection method for AFB1 using a novel humanoid-shaped fiber optic WaveFlex biosensor (refers to a plasmon wave-based fiber biosensor). The fiber probe has been functionalized with nanomaterials (gold nanoparticles, graphene oxide and multiwalled carbon nanotubes) and anti-AFB1 antibodies to enhance the sensitivity and specificity of the developed sensor. The findings demonstrate that the developed sensor exhibits a remarkable low detection limit of 34.5 nM and exceptional specificity towards AFB1. Furthermore, the sensor demonstrated exceptional characteristics such as high stability, selectivity, reproducibility, and reusability. These essential factors highlight the significant potential of the proposed WaveFlex biosensor for the accurate detection of AFB1 in diverse agricultural and food samples.

1. Introduction

Natural-occurring toxins are generally tasteless, stable, odorless, and colorless chemical compounds released from certain organisms as a response to adverse conditions. It has a threatening effect on human life, and high concentration exposure can cause death, whereas low concentration induces chronic health effects [1]. Aflatoxin is a secondary metabolite with high toxicity, naturally produced from *Aspergillus*. *Aspergillus* growth can be significantly enhanced in warm and humid parts of the world. It is very difficult to completely eradicate *Aspergillus* due to spore spreading by asexual reproduction. It has been observed that conditions get worse during the pre-harvest time, which is enhanced in the post-harvest condition because of poor transportation and storage conditions [2]. Thus, warm and humid conditions promote *Aspergillus* growth, whereas drought conditions induce the production of aflatoxin (AFB1), which leads to a vicious fungal and toxin infection cycle [3]. Among all aflatoxins, aflatoxin B1 (AFB1) exhibited carcinogenic potential and was considered the most hazardous compound [4]. Due to its high environmental stability, AFB1 causes severe food contamination and can be bioaccumulated to a greater extent in the environment as well. Aflatoxicosis is the general term used for the disease caused by AFB1. It can be significantly absorbed in the blood, cross the placenta, cause damage to primary organs like the liver, and induce symptoms like abdominal pain, vomiting, and nausea. Its chronic exposure induces severe health complications like liver cancer, teratogenicity, and immunotoxicity [5]. It has been well reported that the lethal doses for animals, children, and humans are 0.5–10 mg, 3 mg, and 10–20 mg/kg body weight, respectively [6]. European Legislation 574/2011/EC

#500311 https://doi.org/10.1364/BOE.500311
Journal © 2023 Received 11 Jul 2023; revised 28 Jul 2023; accepted 4 Aug 2023; published 10 Aug 2023

Biomedical Optics EXPRESS

mentioned that for dairy and young animals, the maximum AFB concentration should be 5 µg/kg, whereas for other complementary and completed feeds, it should be 10 µg/kg [7,8]. Apart from health risks, AFB1 exposure also causes major economic losses by reducing the grain value as an export item as well as animal feed [9]. According to the Food and Agriculture Organization (FAO), nearly 25% of crops around the world have been contaminated with AFB1, that leads to billion-dollar losses [10]. During export, the maximum residue limit (MRL) of aflatoxin will be tested, and if it rises above the MRL value, shipment will be rejected, which leads to huge economic losses. Rapid Alert System for Food and Feed (RASFF) reported that, between 2015 and 2020, most of the mycotoxin contamination was due to aflatoxin [11]. Thus, in recent times, there has been an urgent requirement for more accurate, rapid, and convenient methods for aflatoxin detection by food forensicists. A very low AFB concentration in ppb can induce toxicity, thus requiring highly sensitive techniques for its detection. High-pressure liquid chromatography (HPLC), enzyme-linked immunosorbent assay (ELISA), mass spectrometry, and liquid chromatography are some major techniques to analyze its concentration. However, these techniques have several limitations, including being time-consuming, highly costly, and requiring special training for operation [12]. In order to overcome these problems, fiber optic biosensors came into existence due to their easy operation, high sensitivity, and cartridge-like disposability [13]. It mainly works on the principle of receiving more evanescent waves (EWs) to stimulate (localized) surface plasmon resonance (SPR/LSPR) phenomena. SPR-based biosensors have found extensive applications in various biological and life science fields [14]. Within optical fiber sensors, the simple design of a tapered optical fiber enables direct detection of both individual bacteria [15] and multiple cells [16]. Although, LSPR-based sensors are more cost-effective, sensitive, fast-responsive, and portable for nanoscale biomolecular detection. These sensors primarily work on the detection of changes in refractive index (RI) around them. With the change in RI, peak resonance wavelengths in LSPR spectra also varied, and the concentration of the analyte can be determined in terms of the wavelength shift. Thus, an LSPR-based method is more appropriate for the detection of AFB1 in analytes [17].

Several studies reported the detection of AFB in different formats, like Pal *et al.*'s recent development of the plastic optical fiber (POF) sensor for the detection of AFB1 in the micromolar to picomolar range with reasonably accurate accuracy. Authors have also demonstrated its detection in human serum and urine samples in order to prove its pathological relevance [2]. The recovery result lies between 81% and 117% to demonstrate reasonable accuracy. In another study, Moon *et al.* demonstrated SPR-based on-site detection of AFB1 [18]. The authors have shown a low detection limit of 2.51 ppb and a quantification of 16.32 ppb. This sensor was tested for the presence of AFB1 in almond, rice, and peanut samples, proving its application in on-site detection in the field. However, it has been reported that SPR-based sensors are more expensive and less flexible in comparison to the LSPR method.

Metal nanoparticles (MNPs) like gold nanoparticles (AuNPs) serve as excellent LSPR candidates due to their stable physical and chemical properties. Moreover, the LSPR phenomenon is greatly dependent on the size of nanoparticles (NPs), and thus, in order to excite the LSPR phenomenon, NPs' sizes must be smaller than the wavelength of incident light [19]. Thus, AuNPs have been widely utilized in the development of LSPR based sensors. Moreover, carbon based nanomaterials like graphene oxide and multiwalled carbon nanotubes (GO/MWCNTs) are also extensively used by researchers in optical fiber-based biosensor development due to their unique properties like enhanced conductivity, outstanding optical properties, high energy capacity and large surface area [20].

In recent years, fiber optic sensors have gained significant popularity and have found applications in various fields. For instance, plastic optical fibers have been utilized for remote monitoring of lower limb biomechanics [21]. Zhou *et al.* introduced cantilever assisted fiber-based biosensors

Biomedical Optics EXPRESS

for rapid detection of antibiotic [22]. Additionally, Li *et al.* developed a biosensor using GO-coated double helix microfiber for detection of anti-Müllerian hormone [23]. Various researchers have explored diverse fiber structures for sensor development. For instance, Choudhary *et al.* utilized double cladding fiber (DCF) to develop a RI sensor, achieving impressive sensitivity [24]. Additionally, Esposito *et al.* designed fiber Bragg grating-based sensors for various bio-chemical sensing applications [25,26]. These examples highlight the widespread use of optical fiber-based sensors in different applications. Among the various fiber structures, the WaveFlex biosensor has recently emerged as a notable innovation. The term "WaveFlex biosensor" refers to a plasmon wave-based fiber biosensor known for its flexibility and versatility. This innovative biosensor can detect and measure biomolecules with exceptional sensitivity, making it highly impactful across various applications. This type of sensor offers unique advantages and characteristics. Other WaveFlex biosensor's structures, such as periodic taper, dual-taper, double S-taper, taper-in-taper, and multi-taper-in-taper, have also been reported in recent studies [27]. These advancements in fiber optic sensor technology demonstrate the continuous progress and exploration in this field.

Thus, in the present study, a highly sensitive, label-free, specific, and fast detection of AFB1 using a novel humanoid-shaped fiber optic WaveFlex biosensor is developed. The humanoid-shaped fiber optic structure has been fabricated and functionalized with AuNPs, GO/MWCNTs, and AFB1 antibodies in order to enhance the sensitivity and specificity. Due to its layered structure, GO/MWCNTs provides a high surface for antibody attachment, thus facilitating the antigen-antibody interaction, whereas AuNPs stimulate the LSPR phenomenon. The presence of both nanomaterials together can greatly enhance the performance of a sensor. The results showed that the developed sensor has a low detection limit of 34.5 nM and high specificity towards AFB1. Thus, the proposed optical fiber-based sensor can be significantly utilized in the sensing of the presence of AFB1 in various agricultural as well as food samples.

2. Experimental section

2.1. Materials

The conventional single-mode fiber (SMF, 8.2/125 µm, Shenzhen Technologies Co., Ltd., China) was used for the fabrication of humanoid-shaped fiber structure. Tetrachloroauric acid ($HAuCl_4$, Merck), and trisodium citrate were used for the synthesis of AuNPs solution. The modified Hummer's method used potassium permanganate ($KMnO_4$), graphite powder, sodium nitrate ($NaNO_3$), hydrochloric acid (HCl), and sulfuric acid (H_2SO_4) for synthesis of GO. The MWCNTs powder was purchased from Xianfeng Nano, China. The N,N-dimethylformamide (DMF) was used to prepare the GO/MWCNTs nanomaterial. The 11-mercaptoundecanoic acid (MUA), ethyl (dimethylaminopropyl) carbodiimide (EDC), 3-thiol-propyl triethoxysilane (MPTMS), and N-hydroxysuccinimide (NHS), were purchased from Sigma-Aldrich, China, and these reagents were used for nanomaterial-immobilization as well as enzyme functionalization. AFB1 and zearalenone were obtained from Macklin, China, while Aflatoxin B2 (AFB2), Aflatoxin G1 (AFG1), bovine serum albumin (BSA), and deoxynivalenol were purchased from Aladdin, China. The anti-aflatoxin B1 antibody was procured from Merck. Phosphate-buffered saline (1×PBS, pH 7.4) buffer from Merck, was utilized for the preparation of various concentrations of AFB1 solutions.

2.2. Instruments

The primary instrument used for the development of humanoid-shaped fiber structure using conventional SMF was the combiner manufacturing system (CMS, USA). Thereafter, a fusion splicer machine (FSM-100P+, Fujikura) and cleaver (CT-32, Fujikura) were used for splicing the fiber sensor probe with the optical source and spectrometer. The absorption spectra of the AuNPs were measured using a UV-visible spectrophotometer (Hitachi U-3310). A tungsten-halogen

Biomedical Optics EXPRESS

light source (HL-2000-LL, Ocean Optics), which emits a wide spectrum of light, was used as an experimental light source. The spectrometer (USB2000+, Ocean Optics) was used to process and record the LSPR spectral data to the computer. A high-resolution transmission electron microscope (HR-TEM, Talos L120C, Thermo Fisher Scientific) was used to obtain the shape and size of AuNPs and GO/MWCNTs. A scanning electron microscope (SEM, Gemini, Carl Zeiss Microscopy) was used to confirm the functionalization of nanomaterials over the fiber surface.

2.3. Sensing mechanism of the probe

In the domain of optical fiber transmission, the principle of total internal reflection (TIR) governs the propagation of light. This phenomenon is intricately related to Snell's law, an equation that depicts the refraction of light as it transitions between different media:

$$n_{co} sin\theta_1 = n_{cl} sin\theta_2 \tag{1}$$

Here, n_{co} and n_{cl} are the RI of the core and clad of fiber, respectively. And θ_1 and θ_2 are incidence and refraction angles. In accordance with the principle of TIR, light can be transmitted without any loss, if incidence angle exceeds critical angle.

The EWs are decaying electromagnetic waves generated by the fiber core and propagating towards the cladding surface as shown in Fig. 1. This equation can be used to characterize the evanescent field [27]:

$$E = E_0 exp\left(-\frac{\delta}{d_p}\right) \tag{2}$$

here, E_0 is the field strength and δ represents the distance from the core-cladding interface. The strength of EWs decay to *1/e* from core to cladding surface. The penetration depth (d_p) of EWs can be:

$$d_p = \frac{\lambda}{2\pi\sqrt{n_{cl}^2 \sin^2\alpha - n_{en}^2}} \tag{3}$$

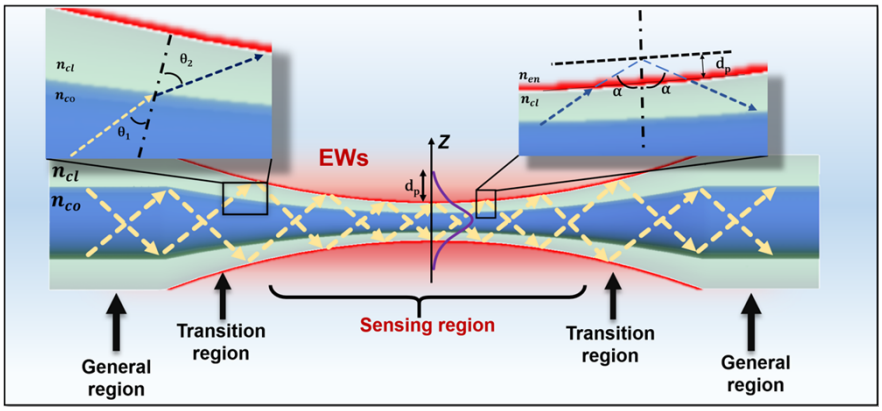

Fig. 1. Light propagation through conventional taper fiber, adapted from [27].

Here, α represents the angle of incidence of light at the interface between the fiber cladding and the external environment. λ denotes the wavelength of the incident light. n_{cl} and n_{en} correspond to the RIs of the fiber cladding and the external environment, respectively.

The tapered fiber offers several advantages over the traditional TIR transmission mode. It provides a larger mode field, broader spectral range, and facilitates the excitation of EWs, as

Biomedical Optics EXPRESS

shown in Fig. 1 [27]. In the case of the localized SPR phenomenon, the resonance wavelength can be mathematically expressed as:

$$\lambda_{res} = \lambda_w \sqrt{2n_e^2 + 1} \tag{4}$$

here, λ_w is the bulk metal plasma wavelength. When the RI of the dielectric on the metal layer's surface is altered, it leads to a new resonance wavelength. This change can be described macroscopically as a variation in the resonance wavelength. The change in the resonance wavelength can be expressed using Eq. (5) [27].

$$\Delta\lambda_{res} = S\Delta n_d \left[1 - exp\left(-\frac{2d}{l_d}\right)\right] \tag{5}$$

here, Δn_d is the change in the RI of surrounding environment, S denotes the bulk RI response of NPs, l_d is the attenuation length of the characteristic electromagnetic field, and d represents the effective adsorption. By incorporating a tapered structure in an optical fiber, a greater number of optical fields are excited as the core and cladding diameters decrease. This results in the generation of high EWs on the outer surface of the cladding. In the context of biosensing, a novel humanoid-shaped fiber structure was developed and evaluated. The unique shape of this tapered region is particularly effective in exciting the field in the sensing region and generating higher-power EWs, surpassing the capabilities of conventional tapered structures. Additionally, the humanoid-shaped fiber structure offers a larger surface area compared to traditional tapered fibers, thereby increasing the contact area between the EWs and the surrounding environment. Thus overall, humanoid-shaped fiber structure incorporates multiple taper treatments, surpassing the conventional single-taper design [28,29]. This innovation expands the sensing region, generating a stronger evanescent field, and offers ample space for nanomaterials and enzyme functionalization.

2.4. Fabrication of sensor probe

The fabrication of the humanoid-shaped fiber structure was achieved using the combiner manufacturing system (CMS) machine. The CMS machine offers unique thermal stability, allowing for the smooth and repeatable development of humanoid-shaped fiber structure using conventional SMF. By employing a thermally stable technique, the CMS generates a uniform plasma field around the optical fiber, resulting in an ultra-low-loss humanoid-shaped fiber structure. The CMS machine operates in a three-electrode mode, effectively covering the entire fiber surface. It is a fully computerized system with various tapering programs available to produce different tapering structures. The tapering properties, such as waist length and waist diameter, are controlled by parameters like waist power, initial power, vacuum value, and operating speed. Optimal parameter settings are necessary to ensure the production of the most repeatable fiber structure. Before tapering, the fiber undergoes pretreatment, which involves the removal of the coating from the center part of the fiber and cleaning the fiber surface using ethanol. Calibration of the CMS machine is essential prior to aligning the fiber structure for tapering. Alignment is accomplished by securing the glass tubes at both ends with fiber optic clamps, thereby ensuring that the vertical and horizontal positions as well as pitch angle are identical on both sides of the platform. The schematic of the humanoid-shaped fiber structure, is depicted in Fig. 2. This structure is primarily controlled by two programs: Program 1 (initial diameter 125 µm, waist diameter 40 µm) and Program 2 (initial diameter 125 µm, waist diameter 60 µm).

2.5. Synthesis process of AuNPs, and GO/MWCNTs

The Turkevich method [30] was used to synthesize AuNPs. This is a well-known method that involves using trisodium citrate as the reducing agent to reduce $HAuCl_4$ to prepare AuNPs. The

Biomedical Optics EXPRESS

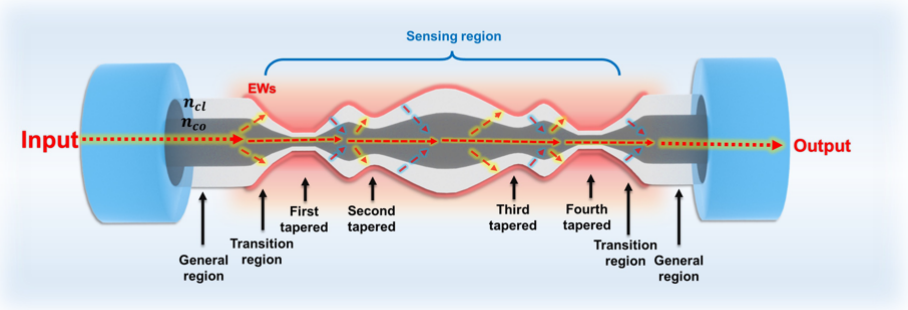

Fig. 2. Schematic of humanoid-shaped fiber-based sensor structure.

specific procedures can be categorized into three distinct components. Initially, a volume of 14.85 mL of deionized water and 150 µL of tetrachloroauric acid (100 mM) were subjected to the boiling process. Next, a solution of trisodium citrate (38.8 mM, 1.8 mL) was swiftly introduced to facilitate the reduction reaction, necessitating a period of five minutes during which heating and stirring were employed. Subsequently, the heating apparatus was switched-off, and the mixture was stirred for ten minutes.

The modified Hummer's method was utilized to synthesize GO nanosheets in this study [31]. The subsequent methodology was employed in the preparation of the hydride solution containing GO and MWCNTs [20]. A mixture was prepared by combining 12.5 mg of GO powder with 37.5 mg of MWCNTs in 100 mL of DI water using a magnetic stirrer. Subsequently, a volume of 1 mL of hydrazine solution and 7 mL of ammonia solution were introduced into the mixture, which was continuously stirred and heated at a temperature of 80 °C for a duration of 30 min. Afterwards, the blender was removed, and the solution was immersed in a water bath maintained at a temperature of 90 °C for 30 min. Following the completion of the bath treatment, the solution was subjected to centrifugation at a speed of 3500 rpm for 1 hour. Upon the completion of the collection process, the turbid supernatant was carefully transferred into a petri dish and subsequently subjected to a drying procedure. This meticulous process resulted in the acquisition of the pulverized powder, consisting of GO and MWCNTs. The synthesized GO/MWCNTs were dispersed using DMF to obtain 0.5 mg/mL nanocomposites, followed by sonication of the dispersed solution.

2.6. Nanocoating and enzyme functionalization

Before nanocoating, the optical fiber surface was cleaned with acetone for 20 minutes to remove organic contamination, then treated with Piranha solution (30% H_2O_2: H_2SO_4 3:7) for 30 minutes, and dried to form hydroxyl groups, which facilitate the nanomaterials' conjugation.

Thereafter, the probe was immersed in coupling agent, *i.e.*, MPTMS, for 12 hours for the formation of the SH group, which helps in AuNPs immobilization. AuNPs and GO/MWCNTs were immobilized on the fiber surface via the dip-coating method [32]. Firstly, the probe was immersed in AuNPs solution for 48 hours, followed by rinsing with ethanol to remove unbound AuNPs and drying with N_2 gas. Next, the probe was functionalized with GO/MWCNTs via the annealing method, which provides an attachment site for antibodies, as shown in Fig. 3. AFB1 antibody functionalized the fiber surface via covalent bonding. Nanomaterials-coated fiber probes were immersed in an ethanolic MUA solution (0.5 mM) for 5 hours to form a carboxylic surface at the surface. Further, the probe was immersed in 200 mM EDC and 50 mM NHS solutions for 30 min to activate the carboxylic group, which can strongly interact with the amino group present in the AFB1 antibody via covalent bonding, as shown in Fig. 3. Fiber was dipped

Biomedical Optics EXPRESS

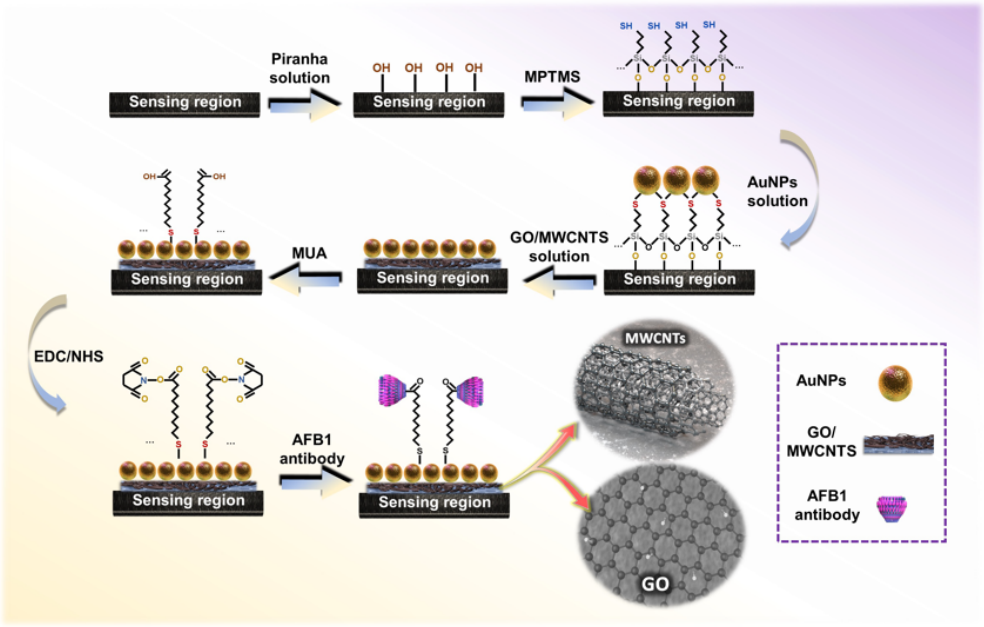

Fig. 3. Nanoparticles-immobilization and enzyme functionalization over the fiber structure.

in an anti-aflatoxin B1 antibody solution for 12 hours and then used for the measurement of different concentrations of analytes.

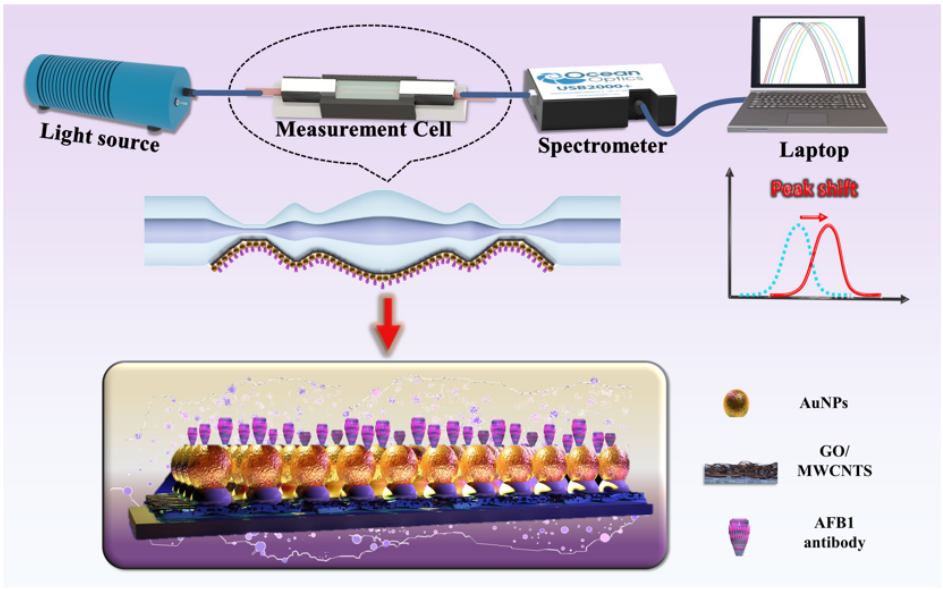

Fig. 4. Experimental setup for aflatoxin measurement using the humanoid-shaped fiber sensor.

Biomedical Optics EXPRESS

2.7. Preparation of analytes solutions

AFB1 solutions of different concentrations, *i.e.*, 20, 50, 100, 200, 300, 400, and 500 nM were prepared using 1× PBS. Firstly, prepared the stock solution of 500 nM, then diluted the solution using 1× PBS to get the lower concentration. The performance of the proposed humanoid-shaped fiber structure was evaluated using AFB1 sample solutions with concentrations ranging from 0 to 500 nM.

2.8. Experimental setup

Figure 4 shows the experimental setup for the detection of AFB1 solutions. The LSPR effect was induced by tungsten-halogen light sources having a 200–1000 nm wavelength. Further, spectrometer collected LSPR spectra and transmitted them to computer, which convert them into text format for data processing. The optical fiber probe was connected to the optical path via the fusion splicer machine and fixed with a clamp.

3. Results and discussions

3.1. Simulation results

To simulate the light propagation through the proposed humanoid-shaped fiber structure, the RSoft software was utilized. The simulation model was constructed in RSoft CAD, following the experimental setup described in the study. A conventional SMF with a core diameter of 8.2 µm and a cladding diameter of 125 µm was considered for the simulation. The RIs of the core and cladding were set to 1.4504 and 1.4447, respectively, while the background RI was set to 1 and excitation wavelength is 1550 nm. The simulation result of the proposed humanoid-shaped fiber structure is presented in Fig. 5(a). In this figure, "1, Launch" represents the total energy distribution of the light source incident on the core, "1, Mode 0" represents the energy distribution of the propagation modes in the core, and "2, Mode 0" represents the energy distribution of the propagation modes in the cladding. From Fig. 5(b), it can be observed that as the light passes through the taper region, the energy of the core mode experiences a significant decrease, while the energy of the cladding mode undergoes a substantial increase. This phenomenon leads to the predominant propagation mode in the taper region being the cladding mode. Additionally, continuous coupling occurs between the core mode and the cladding mode, resulting in oscillations in the energy distribution within the taper region. The simulation results demonstrate that the proposed humanoid-shaped fiber structure has the capability to excite strong cladding modes, which is advantageous for generating EWs.

3.2. Optimization of the optical fiber sensor probe

The CMS machine provides comprehensive computerized control, allowing for the optimization of tapering parameters such as taper waist diameter, electrode power, motor speed, and more. Proper optimization of these parameters is crucial to achieve highly repeatable and novel taper fiber structures. The diameter of the taper fiber and its flexible structure play a significant role in sensing improvement. While a lower diameter can enhance the excitation of EWs and improve sensing capabilities, it also makes the tapered fibers more fragile. Therefore, in this study, we have optimized and selected a waist diameter of 40 µm and 60 µm for the fibers. The resulting structure of the tapered fibers resembles a human shape, leading to their designation as "Humanoid Shaped Optical Fiber Structure". The diameter scan of the fabricated humanoid-shaped fiber structure is presented in Fig. 6(a), demonstrating the variations in diameter along the taper. Additionally, Fig. 6(b) displays the normalized intensity spectra of the fabricated fiber structures. Figure 6 reveals that the fabricated structures exhibit high repeatability, ensuring consistent and identical sensing capabilities.

Biomedical Optics EXPRESS

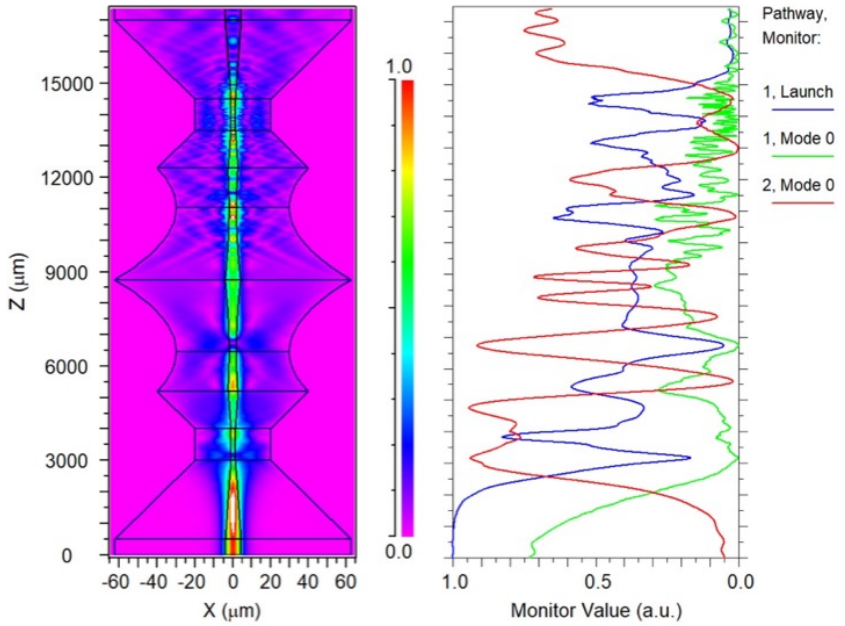

Fig. 5. Simulation results of humanoid-shaped fiber structure.

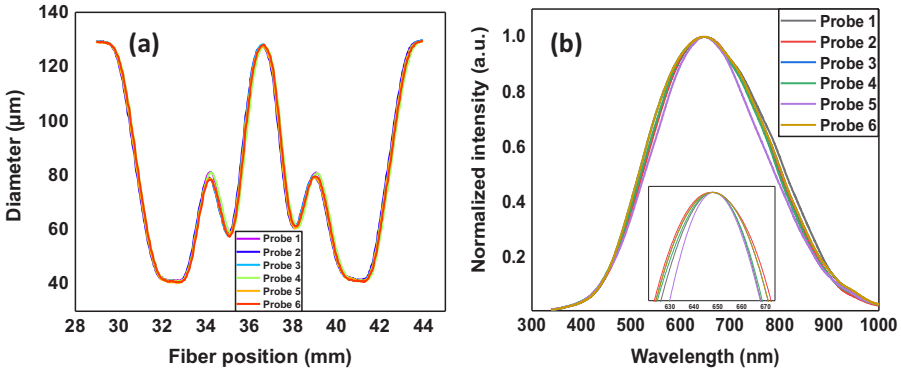

Fig. 6. Repeatability analysis of the fabricated humanoid sensor structure: (a) diameter scanning result obtained through CMS machine; (b) normalized intensity spectra of the fabricated probe.

Biomedical Optics EXPRESS

3.3. Characterization of nanoparticles

The characterization of AuNPs has been conducted using HRTEM and UV-visible spectrophotometer. The TEM results demonstrates that synthesized AuNPs are uniform, spherical in shape, and have an approximate 10 nm diameter, as shown in Fig. 7(a).

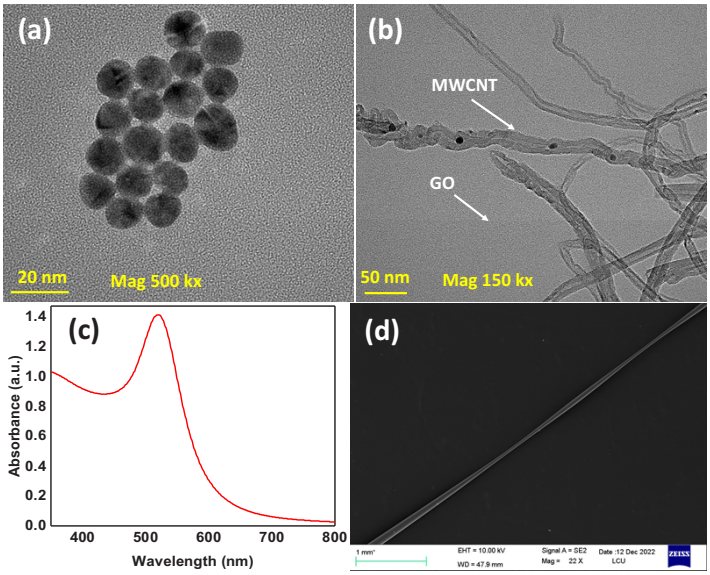

Fig. 7. HR-TEM images of (a) AuNPs, (b) GO/MWCNTs, (c) absorbance spectra of AuNPs, and (d) SEM images of a developed humanoid-shaped fiber sensor structure.

Further, GO/MWCNTs characterization is achieved by HRTEM, as shown in Fig. 7(b). The results display that the GO used in this experiment exhibits a thin layer structure with enhanced surface area. Here, the higher resolution of HR-TEM magnifies the GO sheet, making it appear larger, and the MWCNTs are observed to be situated over the GO sheet. It is shown in Fig. 7(c) that the maximum resonance absorption wavelength of AuNPs lies at 519 nm, which is also in agreement with its size. Figure 7(d) shows the actual image of the humanoid-shaped fiber sensor structure.

3.4. Characterization of the nanomaterial-immobilized structure

SEM is used to confirm the coating of AuNPs and GO/MWCNTs over the fiber probe. It is clear from Fig. 8(a) that AuNPs are uniformly immobilized over the fiber surface, followed by the layered structure of GO/MWCNTs in Fig. 8(b). Therefore, in Fig. 8(c), the energy dispersive spectrum (EDS) analysis of Fig. 8(b) confirms the presence of carbon (C) element, which corresponds to GO/MWCNTs, and gold (Au) element, which corresponds to AuNPs. Additionally, the elements silicon (Si) and oxygen (O) are observed, attributed to the composition of the optical fiber, which is primarily made of silica (SiO_2). This EDS analysis provides valuable insights into the elemental composition and further validates the successful functionalization of the fiber with the respective nanomaterials. This can greatly enhance the surface area of the fiber for antibody immobilization. Thus, with the above results, we can clearly proof the presence of NPs over the fiber surface that can be utilized for the detection of AFB1.

Biomedical Optics EXPRESS

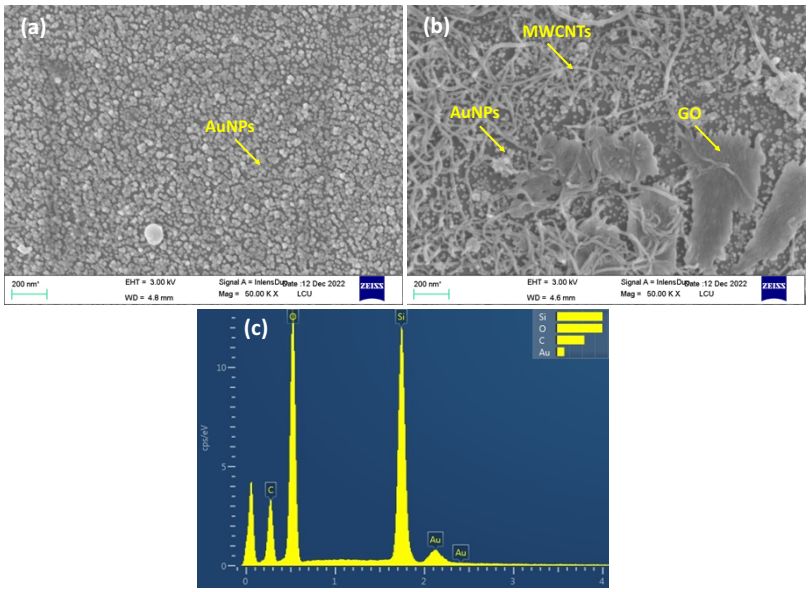

Fig. 8. (a) AuNPs-immobilized over fiber structure, (b) AuNPs, and GO/MWCNTs-over the fiber probe, (c) EDS analysis of Fig. 8(b).

3.5. Measurement of analytes

Different AFB1 concentrations ranging from 20-500 nM are prepared to prove the working of our developed sensor probe. In order to nullify the false effect, LSPR spectra from low to high concentrations of AFB1 have been detected with the setup. The probe was washed with PBS before starting the measurement of the new concentration to minimize the experimental error. The dielectric property of the surrounding medium generally governs the LSPR resonance property of the probe produced due to the presence of AuNPs at its surface [33]. LSPR spectra for the detection of different AFB1 concentrations have been shown in Fig. 9(a). It can be clearly observed that with an increase in AFB1 concentration, there is a clear red shift in the LSPR spectrum. It can be concluded that different concentrations of AFB1 induce RI changes in the surrounding medium of the sensor probe, thus showing the LSPR spectrum drift. The detection limit, sensitivity, and linear fitting factor of the proposed sensor can be calculated for further analysis of the results. A graph of linear fitting has been shown in Fig. 9(b), with linear fitting Eq. (6):

$$\lambda = 0.0077\ C + 647.31 \tag{6}$$

Here, λ is LSPR spectrum peak resonance wavelength; C represents analyte concentrations. The results show the linear fitting factor $R^2 = 0.9669$, with a linear detection range of 0-500 nM.

Detection limit is the most crucial factor in the development of any sensor, which can be determined by the standard deviation (SD) of the peak wavelength calculated at lower analyte concentration in stable conditions [34]. From the results, SD is 0.088562, thus the detection limit of the proposed sensor has been calculated to be 34.5 nM, whereas sensitivity is found to be 7.7 nm/μM.

As it has been reported, the World Health Organization (WHO) has set a limit of 48 nM for the exposure of AFB1 to humans and animals, whereas the Chinese National Food Safety Commission has set the maximum standard level at 64 nM [35,36]. Thus, our developed sensor can efficiently detect AFB1 within the limit set by authorities.

Biomedical Optics EXPRESS

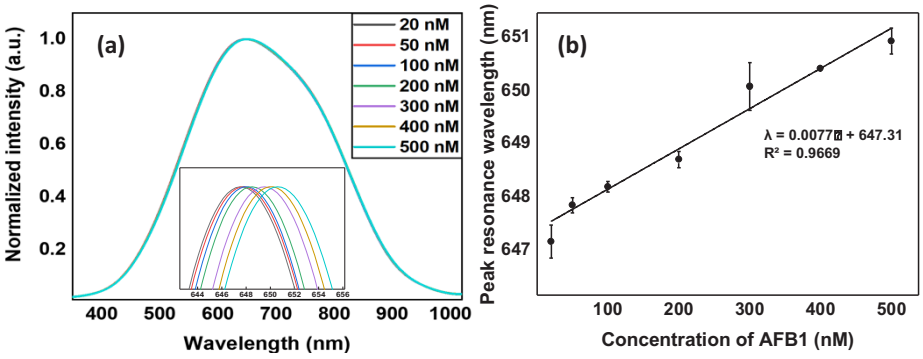

Fig. 9. (a) Sensing spectrum and (b) linear plot of developed sensor.

3.6. Stability and pH test

Stability is another crucial factor in the development of biosensors. As shown in Fig. 10(a), for a certain period of time, the initial wavelength position remains the same, thus illustrating the excellent stability of the developed sensor. The LSPR spectra peak wavelength of the developed sensor has been recorded with 1×PBS for fifteen times simultaneously. The results show that after fifteen consecutive measurements, only a small SD of 0.088 is observed in peak wavelength shift, which further establishes the stability of the sensor.

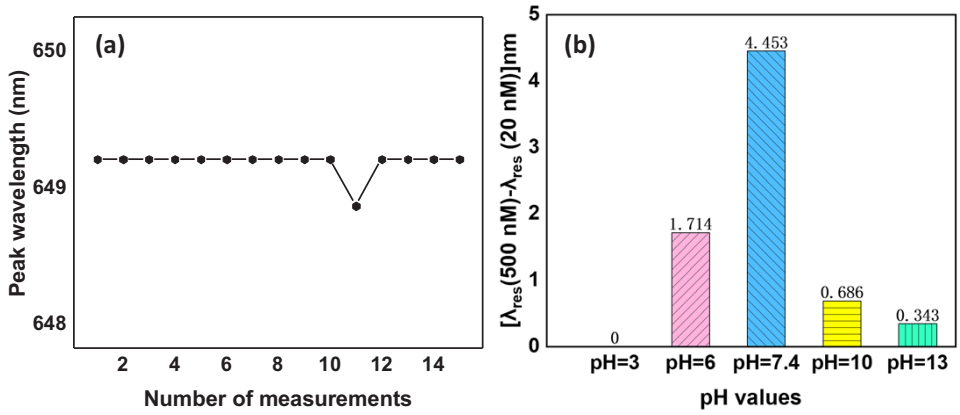

Fig. 10. Performance analysis, (a) stability and (b) pH-test of sensor.

Further, we evaluated the functionality of the developed sensor in different pH environments. Solutions of pH 3, 6, 10, and 13 are prepared by using acetic acid, anhydrous ethanol, and potassium hydroxide, respectively. 500 nM AFB1 is dissolved in the above-prepared solutions to validate the detection process. As shown in Fig. 10(b), the highest LSPR wavelength shift is obtained at pH 7.4 in comparison to other pH conditions. Thus, it can be concluded that the developed sensor works suitably at pH 7.4 in PBS solvent. The performance of the anti-aflatoxin B1 antibody at pH 7.4 is better during the detection of aflatoxin using an optical fiber sensor due to its optimal binding affinity and stability at this specific pH level. At pH 7.4, the antibody's structure and active sites are ideally suited for interacting with the aflatoxin molecules, leading to a stronger and more specific binding reaction. This pH value mimics the physiological conditions in which the antibody is naturally designed to function, making it more effective in recognizing and capturing aflatoxin molecules. On the other hand, at acidic or basic pH levels (lower or

Biomedical Optics EXPRESS

higher pH values), the conformation of the antibody may undergo changes, affecting its active sites and binding capabilities. At lower pH, the antibody may become denatured or lose its shape, leading to a decrease in binding efficiency and lower detection sensitivity. Similarly, at higher pH levels, the antibody's structure may be altered, rendering it less effective in binding with aflatoxin molecules. In summary, the anti-aflatoxin B1 antibody works better at pH 7.4 during aflatoxin detection because it is optimized to function at this specific pH, providing higher sensitivity and specificity. This pH also corresponds to most human fluids, thus confirming the suitability of the developed sensor in real-life clinical applications. Deviations from this pH range can negatively impact the antibody's binding affinity, resulting in lower or inactive performance in aflatoxin detection.

3.7. Reproducibility and reusability test

Reproducibility and reusability are two crucial factors in evaluating the measurement performance of any sensor. Reproducibility can be defined as whether two different fibers exhibit the same sensing performance, whereas reusability is defined as whether the same optical fiber produces the same sensing result when tested for the same concentration repeatedly at different times. In our study, we tested the 100 nM AFB1 solution to follow the reproducibility results of the developed sensor. Three different probes are used to test the concentration of AFB1, and as shown in Fig. 11(a), the recorded intensity for all the probes is the same. Thus, it can be concluded that the developed sensor exhibited excellent reproducibility parameters.

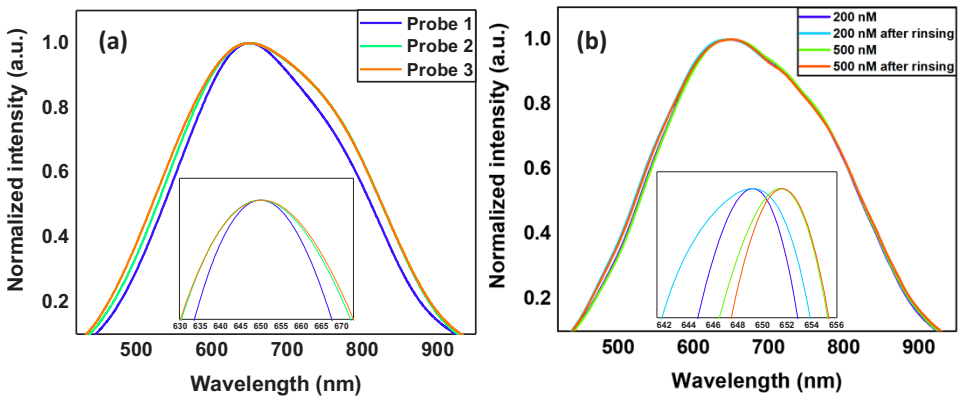

Fig. 11. Performance analysis, (a) reproducibility, (b) reusability test of sensor.

In order to verify the reusability factor, two different concentrations of AFB1, *i.e.*, 200 nM and 500 nM, were tested using the same optical fiber. As shown in Fig. 11(b), sensing curve results are similar for both concentrations in two different measurements, *i.e.*, before and after rinsing the probe with PBS. Thus, it can be proposed that the developed sensor can be reused several times without compromising the quality of the results.

3.8. Selectivity test

Selectivity is one of the most crucial factors of a sensor in order to maintain its real-life application. Thus, the selectivity of the developed sensor has been tested in the presence of different interferents, *i.e.*, AFB2, AFG1, deoxynivalenol, BSA, and zearalenone.

All these interferents generally occur in conjunction with AFB1, thus being selected for the selectivity test of the sensor. Firstly, the peak wavelength of a 20 nM AFB1 solution has been measured as a control. Thereafter, peak resonance wavelength shifts are recorded for each interferent at the 500 nM concentration. As shown in Fig. 12, there is a significant change in peak

Biomedical Optics EXPRESS

wavelength only in the presence of AFB1, whereas other analytes did not induce any significant change. The presence of AFB1 antibody over the sensor probe is responsible for the selectivity of the sensor, which only has specific recognition for AFB1 in comparison to other analytes. Thus, from the results, it can be concluded that the developed sensor exhibited high specificity and recognition ability towards the AFB1 analyte.

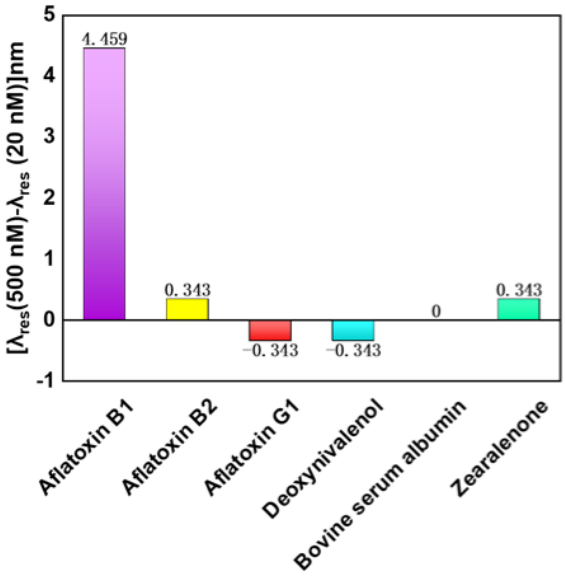

Fig. 12. Selectivity test of the proposed WaveFlex biosensor.

3.9. *Evaluation of sensing performance*

In the present work, an WaveFlex biosensor is developed for detection of AFB1 analyte. Various results confirm the excellent sensing performance of the developed sensor.

This sensor exhibited excellent properties like high stability, reusability, reproducibility, and portability. A comparison of the sensing performance of various reported sensors with the present in terms of sensitivity, detection limit, and linear range are mentioned in Table 1.

Table 1. Performance comparison of proposed sensor with existing AFB1 sensors.

Mechanism	Materials used	Linear range	Sensitivity	LoD	Ref.
SPR	Molecularly imprinted polymers/AuNPs	0.32 pM - 30 nM	n.r.[a]	3.3 pM	[37]
SERS	Cu_2O@Au NCs	0.001-100 ng/mL	n.r.[a]	0.7 pg/mL	[38]
Absorbance	Polyaniline	0.05 - 500 ppb	n.r.[a]	0.112	[2]
Colorimetric	AgNPs	0.64 - 19.21 nM	n.r.[a]	0.288 nM	[39]
SPR	Au	10 - 10000 ppb	n.r.[a]	2.51 ppb	[18]
Reflectance	n.r.[a]	0 - 5 µg/mL	-0.755 µs/ (µg/mL)	0.016 µg/mL	[40]
LSPR	AuNPs/GO/MWCNTs	0 - 500 nM	7.7 nm/µM	34.5 nM	This work

[a]not reported

Biomedical Optics EXPRESS

4. Conclusion

This study describes the development of a highly sensitive, specific, label-free, and rapid method for detecting AFB1 using a novel humanoid-shaped fiber optic WaveFlex biosensor. To improve the sensitivity and specificity of the sensor device, nanomaterials (AuNPs, and GO/MWCNTs) and anti-AFB1 antibodies are incorporated. The results demonstrate that the developed sensor has a remarkable low detection limit of 34.5 nM and remarkable specificity towards AFB1. In addition to its high stability, selectivity, reproducibility, and reusability, the sensor is ideally suited for the precise detection of AFB1 in a wide range of agricultural and food samples. This study contributes to the field of optical sensing by introducing a novel humanoid-shaped WaveFlex biosensor and demonstrating its efficacy in detecting AFB1. The incorporation of nanomaterials into the sensor probe improves its efficacy and sensitivity. The developed sensor features label-free detection, rapid response, and high accuracy, among other advantages. Potential applications of the proposed sensor in food safety and quality control are considerable. Its ability to detect AFB1 in low concentrations makes it an invaluable tool for detecting food contamination and ensuring consumer safety. The sensor's reliability, reproducibility, and reusability make it applicable for use in a variety of situations. Expanding the capabilities of the sensor to detect additional mycotoxins and contaminants can be the focus of future research. The development of portable and user-friendly devices based on this technology has the potential to revolutionize the field of food safety testing by enabling rapid and accurate on-site analysis. The development of the humanoid-shaped fiber optic WaveFlex biosensor for the detection of AFB1 represents a promising solution for food safety monitoring. The sensor's elevated sensitivity, specificity, and other favorable characteristics render it a valuable instrument for researchers, experts in food forensics, and regulatory agencies tasked with the responsibility of guaranteeing the quality and safety of food products.

Funding. Natural Science Foundation of Shandong Province (ZR2020QC061); Liaocheng University (318052341); Double-Hundred Talent Plan of Shandong Province, China; Special Construction Project Fund for Shandong Province Taishan Mountain Scholars.

Disclosures. The authors declare that they have no known competing for financial interests or personal relationships that could have appeared to influence the work reported in this paper.

The authors declare no conflicts of interest.

Data availability. Data underlying the results presented in this paper are not publicly available at this time but may be obtained from the authors upon reasonable request.

References

1. L. Joseph Owuor, O. Solomon, and A. O. O. Dora, "Aflatoxin B1: Chemistry, Environmental and Diet Sources and Potential Exposure in Human in Kenya," in *Aflatoxin B1 Occurrence, Detection and Toxicological Effects*, L. Xi-Dai, ed. (IntechOpen, Rijeka, 2019), Chap. 1.
2. T. Pal, S. Aditya, T. Mathai, and S. Mukherji, "Polyaniline coated plastic optic fiber biosensor for detection of aflatoxin B1 in nut, cereals, beverages, and body fluids," Sens. Actuators, B **389**, 133897 (2023).
3. B. Mousavi, M. T. Hedayati, N. Hedayati, M. Ilkit, and S. Syedmousavi, "Aspergillus species in indoor environments and their possible occupational and public health hazards," Curr. Top. Med. Mycol. **2**(1), 36–42 (2016).
4. D. Bartolić, D. Mutavdžić, J. M. Carstensen, S. Stanković, M. Nikolić, S. Krstović, and K. Radotić, "Fluorescence spectroscopy and multispectral imaging for fingerprinting of aflatoxin-B1 contaminated (Zea mays L.) seeds: a preliminary study," Sci. Rep. **12**(1), 4849 (2022).
5. S. Marchese, A. Polo, A. Ariano, S. Velotto, S. Costantini, and L. Severino, "Aflatoxin B1 and M1: Biological Properties and Their Involvement in Cancer Development," Toxins **10**(6), 214 (2018).
6. L. Afsah-Hejri, S. Jinap, P. Hajeb, S. Radu, and S. Shakibazadeh, "A review on mycotoxins in food and feed: Malaysia case study," Compr. Rev. Food Sci. Food Saf. **12**(6), 629–651 (2013).
7. I. F. M. Almeida, H. M. L. Martins, S. M. O. Santos, M. S. Freitas, J. M. G. N. da Costa, and F. M. d' Almeida Bernardo, "Mycobiota and aflatoxin B1 in feed for farmed sea bass (Dicentrarchus labrax)," Toxins **3**(3), 163–171 (2011).
8. J. J. Tsafack Takadong, H. T. Mouafo, L. Manet, A. Baomog, J. J. Adjele, E. K. Medjo, and G. N. Medoua, "Assessment of the presence of total aflatoxins and aflatoxin B1 in fish farmed in two Cameroonian localities," Int. J. Food Sci. **2020**, 1–6 (2020).

Biomedical Optics EXPRESS

9. J. C. Fountain, P. Khera, L. Yang, S. N. Nayak, B. T. Scully, R. D. Lee, Z.-Y. Chen, R. C. Kemerait, R. K. Varshney, and B. Guo, "Resistance to Aspergillus flavus in maize and peanut: Molecular biology, breeding, environmental stress, and future perspectives," The Crop J. **3**(3), 229–237 (2015).
10. A. Alshannaq and J.-H. Yu, "Occurrence, toxicity, and analysis of major mycotoxins in food," Int. J. Environ. Res. Public Health **14**(6), 632 (2017).
11. A. Alshannaq and J.-H. Yu, "Analysis of EU rapid alert system (RASFF) notifications for aflatoxins in exported US food and feed products for 2010–2019," Toxins **13**(2), 90 (2021).
12. A. P. Wacoo, D. Wendiro, P. C. Vuzi, and J. F. Hawumba, "Methods for detection of aflatoxins in agricultural food crops," J. Appl. Chem. **2014**, 1–15 (2014).
13. S. Chandra, A. Dhawangale, and S. Mukherji, "Hand-held optical sensor using denatured antibody coated electro-active polymer for ultra-trace detection of copper in blood serum and environmental samples," Biosens. Bioelectron. **110**, 38–43 (2018).
14. H. Xin, B. Namgung, and L. P. Lee, "Nanoplasmonic optical antennas for life sciences and medicine," Nat. Rev. Mater. **3**(8), 228–243 (2018).
15. H. Xin, Y. Li, D. Xu, Y. Zhang, C.-H. Chen, and B. Li, "Single upconversion nanoparticle–bacterium cotrapping for single-bacterium labeling and analysis," Small **13**(14), 1603418 (2017).
16. T. Pan, D. Lu, H. Xin, and B. Li, "Biophotonic probes for bio-detection and imaging," Light: Sci. Appl. **10**(1), 124 (2021).
17. K. A. Willets and R. P. Van Duyne, "Localized surface plasmon resonance spectroscopy and sensing," Annu. Rev. Phys. Chem. **58**(1), 267–297 (2007).
18. J. Moon, J. Byun, H. Kim, E.-K. Lim, J. Jeong, J. Jung, and T. Kang, "On-Site Detection of Aflatoxin B1 in Grains by a Palm-Sized Surface Plasmon Resonance Sensor," Sensors **18**(2), 598 (2018).
19. A. J. Haes and R. P. Van Duyne, "A Nanoscale Optical Biosensor: Sensitivity and Selectivity of an Approach Based on the Localized Surface Plasmon Resonance Spectroscopy of Triangular Silver Nanoparticles," J. Am. Chem. Soc. **124**(35), 10596–10604 (2002).
20. R. Singh, Z. Wang, C. Marques, R. Min, B. Zhang, and S. Kumar, "Alanine aminotransferase detection using TIT assisted four tapered fiber structure-based LSPR sensor: From healthcare to marine life," Biosens. Bioelectron. **236**, 115424 (2023).
21. L. Avellar, A. Frizera, and A. Leal-Junior, "POF Smart Pants: a fully portable optical fiber-integrated smart textile for remote monitoring of lower limb biomechanics," Biomed. Opt. Express **14**(7), 3689–3704 (2023).
22. J. Zhou, J. Huang, H. Huang, C. Zhao, M. Zou, D. Liu, X. Weng, L. Liu, J. Qu, L. Liu, C. Liao, and Y. Wang, "Fiber-integrated cantilever-based nanomechanical biosensors as a tool for rapid antibiotic susceptibility testing," Biomed. Opt. Express **14**(5), 1862–1873 (2023).
23. Y. Li, B. Luo, Y. Liu, S. Wu, S. Shi, H. Chen, and M. Zhao, "Microfluidic immunosensor based on a graphene oxide functionalized double helix microfiber coupler for for anti-Müllerian hormone detection," Biomed. Opt. Express **14**(4), 1364–1377 (2023).
24. S. Choudhary, F. Esposito, L. Sansone, M. Giordano, S. Campopiano, and A. Iadicicco, "Lossy mode resonance sensors in uncoated optical fiber," IEEE Sens. J. **23**(14), 15607–15613 (2023).
25. F. Esposito, "(INVITED)Chemical sensors based on long period fiber gratings: A review," Results in Opt. **5**, 100196 (2021).
26. F. Esposito, S. Campopiano, and A. Iadicicco, "Miniaturized strain-free fiber Bragg grating temperature sensors," IEEE Sens. J. **22**(17), 16898–16903 (2022).
27. W. Zhang, X. Lang, X. Liu, G. Li, R. Singh, B. Zhang, and S. Kumar, "Advances in Tapered Optical Fiber Sensor Structures: From Conventional to Novel and Emerging," Biosensors **13**(6), 644 (2023).
28. M. Shaimerdenova, T. Ayupova, Z. Ashikbayeva, A. Bekmurzayeva, W. Blanc, and D. Tosi, "Reflector-less shallow-tapered optical fiber biosensors for rapid detection of cancer biomarkers," J. Lightwave Technol. **41**(13), 4114–4122 (2023).
29. M. Sypabekova, A. Aitkulov, W. Blanc, and D. Tosi, "Reflector-less nanoparticles doped optical fiber biosensor for the detection of proteins: Case thrombin," Biosens. Bioelectron. **165**, 112365 (2020).
30. J. Turkevich, P. C. Stevenson, and J. Hillier, "A study of the nucleation and growth processes in the synthesis of colloidal gold," Discuss. Faraday Soc. **11**, 55–75 (1951).
31. S. Kumar, Z. Guo, R. Singh, Q. Wang, B. Zhang, S. Cheng, F.-Z. Liu, C. Marques, B. K. Kaushik, and R. Jha, "MoS2 Functionalized Multicore Fiber Probes for Selective Detection of Shigella Bacteria Based on Localized Plasmon," J. Lightwave Technol. **39**(12), 4069–4081 (2021).
32. A. Ozcariz, I. Martinez, C. R. Zamarreño, and F. J. Arregui, "Development of copper oxide thin film for lossy mode resonance-based optical fiber sensor," in *Proceedings*, (MDPI, 2018), 893.
33. G. Li, Q. Xu, R. Singh, W. Zhang, C. Marques, Y. Xie, B. Zhang, and S. Kumar, "Graphene Oxide/Multiwalled Carbon Nanotubes Assisted Serial Quadruple Tapered Structure-Based LSPR Sensor for Glucose Detection," IEEE Sens. J. **22**(17), 16904–16911 (2022).
34. J. Hromadka, B. Tokay, R. Correia, S. P. Morgan, and S. Korposh, "Highly sensitive volatile organic compounds vapour measurements using a long period grating optical fibre sensor coated with metal organic framework ZIF-8," Sens. Actuators, B **260**, 685–692 (2018).

Biomedical Optics EXPRESS

35. S. Li, X. Zhong, Y. Xu, Y. Zheng, X. Shi, F. Li, S. Guo, and J. Yang, "Smartphone-based reading system integrated with phycocyanin-enhanced latex nanospheres immunoassay for on-site determination of aflatoxin B1 in foodstuffs," Food Chem. **360**, 130019 (2021).
36. Z. Xue, Y. Zhang, W. Yu, J. Zhang, J. Wang, F. Wan, Y. Kim, Y. Liu, and X. Kou, "Recent advances in aflatoxin B1 detection based on nanotechnology and nanomaterials-A review," Anal. Chim. Acta **1069**, 1–27 (2019).
37. S. Akgönüllü, H. Yavuz, and A. Denizli, "SPR nanosensor based on molecularly imprinted polymer film with gold nanoparticles for sensitive detection of aflatoxin B1," Talanta **219**, 121219 (2020).
38. P. Chen, S. Li, C. Jiang, Z. Wang, and X. Ma, "A surface-enhanced Raman scattering aptasensor for output-signal detection of aflatoxin B1 based on peroxidase-like Cu_2O@Au hybrid nanozyme," Food Biosci. **54**, 102885 (2023).
39. J. Lerdsri, C. Thunkhamrak, and J. Jakmunee, "Development of a colorimetric aptasensor for aflatoxin B1 detection based on silver nanoparticle aggregation induced by positively charged perylene diimide," Food Control **130**, 108323 (2021).
40. W. Chen, C. Zhao, B. Mao, H. Chen, and C. Shen, "Detection of Aflatoxin B1 in Food Based on SMF Taper Combined With Fiber Loop Ring Down Technique," IEEE Sens. J. **20**(5), 2446–2451 (2020).